

Enhancing the mechanical properties and corrosion resistance of AISI 440C martensitic stainless steel via laser powder bed fusion and post-processing treatment

Original

Enhancing the mechanical properties and corrosion resistance of AISI 440C martensitic stainless steel via laser powder bed fusion and post-processing treatment / Moheimani, K., Tan, Q., Knibbe, R., Karan, B., Basnayake, A., Heitzmann, M., Wang, F., Wu, T., Saboori, A., Zhang, M.. - In: PROGRESS IN ADDITIVE MANUFACTURING. - ISSN 2363-9512. - (2025). [10.1007/s40964-025-01294-z]

Availability:

This version is available at: 11583/3004239 since: 2025-10-20T08:16:00Z

Publisher:

Springer Science and Business Media Deutschland GmbH

Published

DOI:10.1007/s40964-025-01294-z

Terms of use:

This article is made available under terms and conditions as specified in the corresponding bibliographic description in the repository

Publisher copyright

(Article begins on next page)



Enhancing the mechanical properties and corrosion resistance of AISI 440C martensitic stainless steel via laser powder bed fusion and post-processing treatment

Kiomars Moheimani¹ · Qiyang Tan¹ · Ruth Knibbe¹ · Baibhav Karan¹ · Asanka Basnayake¹ · Michael Heitzmann¹ · Feng Wang² · Tao Wu² · Abdollah Saboori³ · Mingxing Zhang¹

Received: 8 May 2025 / Accepted: 14 August 2025

© The Author(s) 2025

Abstract

As the most typical high-strength stainless steel, the heat-treated AISI 440C steel has low machinability. It is also not weldable due to the high carbon content. Additive manufacturing, specifically laser powder bed fusion (LPBF), offers a promising solution for fabricating near-net shape components with this alloy. To address the limited research on the LPBF of AISI 440C steel, this work investigates the LPBF processability, microstructure and phase evolution of the AISI 440C steel, focussing on the role of post-processing treatments on improving mechanical properties, wear and corrosion resistance compared to its wrought counterpart. Our results indicate that highly dense AISI 440C components with > 99.98% relative density can be produced using optimised LPBF parameters. However, the low martensite start (Ms) temperature of the steel and the fast-cooling feature of the LPBF processing result in the formation of an austenite-dominant microstructure in the as-LPBF-fabricated parts with low strength and hardness. Post-processing treatment is required to enable the martensite transformation. Deep cryogenic treatment (DCT) at -196°C in liquid nitrogen had no effect, so conventional quenching and tempering were used. This facilitated $M_{23}C_6$ carbide precipitation, increased the Ms temperature and promoted martensitic transformation. After the heat treatment, the LPBF-fabricated AISI 440C steel exhibits significant improvements, including an ultimate tensile strength over 2.2 GPa compared with the as-LPBF-fabricated steel, enhanced toughness, doubled elongation (7.6%), and comparable hardness to the wrought counterpart. These improvements are attributed to the higher fraction of retained austenite with refined grains and precipitation of fine carbides. In addition, the heat-treated LPBF steel also exhibits the lowest specific wear rate, and superior corrosion resistance compared with the wrought 440C steel, due to improved passivation from the higher amount of retained austenite and finer carbides. The present results provide a foundation for broadening the practical applications of the AISI 440C steel via additive manufacturing.

Keywords AISI 440C stainless steel · Additive manufacturing · Martensite transformation · High-carbon steels · Wear resistance · Corrosion resistance · Toughness

✉ Kiomars Moheimani
k.moheimani@uq.edu.au

Qiyang Tan
q.tan@uq.edu.au

Ruth Knibbe
ruth.knibbe@uq.edu.au

Baibhav Karan
b.karan@uq.edu.au

Asanka Basnayake
p.basnayake@uq.edu.au

Michael Heitzmann
m.heitzmann@uq.edu.au

Feng Wang
wangfeng02@hbisco.com

Tao Wu
wutao03@hbisco.com

Abdollah Saboori
abdollah.saboori@polito.it

Mingxing Zhang
Mingxing.Zhang@uq.edu.au

¹ University of Queensland, Brisbane, Australia

² HBIS (China), Shijiazhuang, China

³ Integrated Additive Manufacturing Centre, Department of Management and Production Engineering, Torino, Italy

1 Introduction

Wear- and corrosion-resistant materials with high strength are always in high demand in mining, metallurgy, tooling, automobile and other engineering sectors [1–3]. Martensitic stainless steels such as AISI 420 and 440C are typical examples of this type of materials [4–6]. However, their intrinsic brittleness, due to the martensite and large amount of carbides, creates challenges for shaping these steels using conventional forming and machining techniques, particularly when high geometric complexities are required [7, 8]. Metal additive manufacturing (AM), specifically laser powder bed fusion (LPBF), offers a solution to this issue as near-net shape components with intricate geometries can be fabricated [7, 9, 10]. In addition, the rapid cooling rates and multiple thermal cycles associated with AM fabrication result in unique microstructures, such as ultrafine cellular substructures, high dislocation density and non-equilibrium phases such as bainite/martensite in the as-fabricated steel [11–15], providing potential for property enhancement.

Previous studies on AM of martensitic stainless steels have primarily focussed on AISI 420 medium carbon steel (C: 0.15–0.4 wt.%) [7, 9, 10, 16]. This steel was reported to exhibit high AM processability and commendable hardness and corrosion resistance directly after LPBF due to the formation of Cr-containing martensite matrix [10, 17–19]. The mechanical performance can even be further improved (e.g. tensile strength over 1800 MPa) through proper post-processing heat treatment or addition of reinforcement nanoparticles (e.g. TiN or TiC) [7, 10, 16].

Compared with AISI 420, AISI 440C martensitic stainless steel offers superior strength, hardness and wear resistance due to its higher C and Cr contents (C: 0.95–1.2 wt.%, Cr: 16–18 wt.%), positioning it as a prime candidate for high-performance applications [20, 21]. Conventionally processed AISI 440C stainless steel typically features a microstructure composed of twinned plate martensite, retained austenite, and $M_{23}C_6$ and M_7C_3 carbides. This microstructure results in a tensile strength over 2 GPa, hardness over 60 HRC, and a combination of high wear resistance and moderate corrosion resistance [20, 22–27]. As a higher grade and value-added material, AISI 440C presents a more promising candidate in the AM community for broader application markets. However, there has been limited research on the LPBF processing of 440C steel [28–30], and its comprehensive performance in terms of mechanical properties, wear and corrosion resistance remains unexplored. Surprisingly, the as-built 440C reported to predominantly exhibit austenite instead of the anticipated martensite microstructure, resulting in insufficient hardness and strength for a wear-resistant material.

Bang and co-workers [28] attributed this anomaly to the extremely high cooling rates during LPBF, which surpassed the threshold required for martensite transformation, consequently lowering the Ms temperature. However, no experimental data were provided to substantiate this hypothesis. Therefore, further investigation is needed to validate this phenomenon and explore the underlying mechanism.

Moreover, existing research on the AM-fabricated high-strength stainless steels focuses on the mechanical tensile properties, with limited attention to their corrosion behaviour and wear resistance. As mentioned above, as a typical high-carbon martensitic steel, 440C steel is characterised by high wear and good corrosion resistance. Hence, it is essential to explore its wear and corrosion behaviours of AM-fabricated 440C steel due to the difference in microstructure produced during AM compared with its conventionally manufactured counterparts.

This study aims to fill these gaps by thoroughly investigating the phase transformation, microstructural evolution, and the resultant mechanical properties, wear and corrosion resistance of LPBF-fabricated AISI 440C steel in both the as-built condition and various post-heat treatment conditions (cryogenic treatment and quenching). By comparing the results with conventionally processed AISI 440C, this study also highlights the benefits and potential drawbacks of AM for producing this steel. It is expected that the outcome of this work will advance the understanding of the capability of AM in producing high-performance martensitic stainless steels for a wide range of industrial applications.

2 Materials and methods

2.1 Powder feedstock and wrought 440C

The powder used in this study was nitrogen-atomised AISI 440C powder granules, supplied by Sandvik Osprey Ltd, UK. The powder exhibited a particle size range of 15–53 μm and a chemical composition of 0.96% C, 16.8% Cr, 0.65% Mn, 0.5% Mo, 0.1% Ni, 0.5% Si, and Fe balance (in wt.%). As shown in Fig. 1, the powder predominantly comprises spherical particles, with a few non-spherical particles interspersed. The particles exhibit a rough surface texture, attributed to finer powder particles satelliting on coarser ones during the atomisation process. This satelliting effect has been widely reported in gas-atomised metal powders due to collisions between small-sized particles and incompletely solidified large-sized droplets [31–33]. Despite this, the good spherical Shape of the powder particles ensures their excellent flowability during the printing process.

Furthermore, the study utilised wrought (hot rolled) AISI 440C stainless steel (provided by Artisan Supplies,

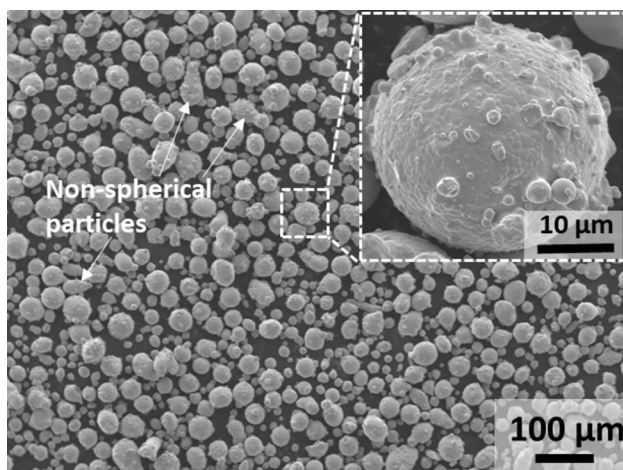


Fig. 1 SEM image of nitrogen-atomised AISI 440C powder

Table 1 Optimised LPBF process parameters for the fabrication of AISI 440C

Process parameter	Value
Laser power (W)	180
Scanning speed (mm/s)	600
Hatching spacing (mm)	0.12
Layer thickness (mm)	0.03

Australia) for comparative research with a chemical composition of 0.98% C, 17% Cr, 0.69% Mn, 0.3% Mo, 0.1% Ni, 0.45% Si, and Fe balance (in wt.%).

2.2 LPBF fabrication of AISI 440C steel

Additively manufactured 440C samples were fabricated using an SLM Solution SLM125HL LPBF system, equipped with an ytterbium fibre laser operating at a wavelength of 1.06 μm and a maximum power of 400 W. The LPBF process parameters were optimised (Table 1) to guarantee a high density of over 99.98% based on a series of preliminary trials (Supplementary Table S.1). The LPBF process was conducted in a high-purity ($\geq 99.99\%$) argon atmosphere, where the oxygen concentration was kept below 0.05 vol.%. All samples were built on a tool steel substrate preheated to 200 $^{\circ}\text{C}$.

2.3 Cryogenic and post-heat treatment processes

The process of deep cryogenic treatment (DCT) involved immersing the as-LPBF-fabricated 440C samples in liquid nitrogen immediately after the LPBF process. This was done for a period of 5 h to ensure that the samples were

uniformly cooled to a temperature of $-196\text{ }^{\circ}\text{C}$. The samples were removed and allowed to gradually return to room temperature following DCT. These samples were labelled as DCT LPBF-fabricated 440C.

The post-processing heat treatment process was conducted in accordance with the standards established in the ASM Handbook Volume 4D, which were specifically designed to enhance the mechanical properties and corrosion resistance of AISI 440C stainless steel [21]. For comparison purposes, the wrought 440C steel samples were also heat-treated. To prevent oxidation, both the wrought 440C samples and the LPBF-fabricated 440C samples were wrapped in stainless steel foils and covered with charcoal. Samples were held at 1065 $^{\circ}$ for 30 min in a muffle furnace, followed by oil quenching. Then the samples were subjected to double tempering at 160 $^{\circ}$ for 30 min. The heat-treated samples were labelled as HT LPBF-fabricated 440C and HT wrought 440C, respectively.

2.4 Phase analysis and microstructure observation

To identify phases in the samples, X-ray diffraction (XRD) patterns were collected using a Bruker D8 Advance diffractometer equipped with $\text{CrK}\alpha$ radiation ($\lambda = 2.28973\text{ \AA}$). This radiation provides superior angular dispersion for phase identification compared to $\text{CoK}\alpha$ or $\text{CuK}\alpha$ radiations. The scanning range was set from 50 $^{\circ}$ to 160 $^{\circ}$ 2 θ , encompassing almost all strong peaks of phases in steels when using $\text{CrK}\alpha$ radiation. The step size was optimised to 0.1 $^{\circ}$ to ensure more than six data points above the full width at half maximum (FWHM), facilitating accurate Rietveld refinement and quantitative phase analysis.

An Olympus DSX1000 Optical Microscope was employed for preliminary microstructural observation to evaluate the densification. A JOEL 7800 field emission scanning electron microscope (FESEM), equipped with both energy-dispersive X-ray spectroscopy (EDS) and electron backscattered diffraction (EBSD) detectors, was used to characterise the detailed microstructures of bulk samples and the morphology of the feedstock powder. Metallographic samples were prepared from the LPBF-fabricated parts by extracting cross-sectional slices along the building direction (BD). These samples were mechanically ground and polished, followed by etching in Amberg's reagent (composed of 1 g CuCl_2 , 20 ml HCl, 65 ml ethanol, and 15 ml distilled water) for 10 s. The grain morphology and texture of each specimen were analysed using EBSD, with a step size of 0.1 μm . To achieve a desired surface finish, the samples were polished for a duration of 3 h using a silica suspension with an abrasive size of 0.06 μm in a Buehler VibroMet 2 vibratory polisher.

2.5 Mechanical and wear testing

Since 440C is used in applications involving wear and impact loading, mechanical testing (including hardness, tensile, and Charpy impact) and wear testing were conducted to evaluate its strength, surface durability and fracture toughness. Rockwell hardness measurements were conducted using a Buehler Macromet tester, with a load of 150 kg and a duration of 10 s. The Rockwell hardness values reported were calculated as the mean of ten measurements obtained from longitudinal sections of the LPBF-fabricated samples and the surface of the HT wrought 440C sample after grinding with SiC sandpapers.

Tensile tests were performed on an Instron 5584 machine with a constant crosshead velocity of 1 mm/min. A video extensometer was used to continuously monitor and measure the strain until the point of fracture. Tensile dog-bone specimens were cut along both longitudinal and transverse directions from the LPBF-fabricated parts using an electro-discharge machine, with gauge dimensions of 16 mm × 3 mm × 2 mm in accordance with the ASTM-E8M-22 standard. For the purpose of comparison, samples of identical size were obtained from HT wrought 440C. To ensure reproducibility, three samples were tested from each set of samples.

Charpy impact tests were performed at ambient temperature using a Mohr & Federhaff A.G. pendulum impact testing apparatus. Charpy impact samples were cut using electro-discharge machining into 10 mm × 10 mm × 55 mm with a central V-notch according to the ASTM-E23-23a standard.

Wear testing was performed using a ball-on-plate apparatus (RTEC MFT2000) in accordance with the guidelines outlined in the ASTM G99–17 standard. Plate samples with dimensions of 50 mm × 50 mm × 10 mm were mechanically ground with 4000 SiC grit sandpapers to obtain an appropriate surface finish. The wear testing was conducted using a rotating setup in direct contact with yttria stabilised zirconia (YSZ) balls (diameter: 10 mm, hardness: > 1250 Hv) that were securely fastened to a stationary holder during the experiment. Before the tests, the ball and samples underwent ultrasonic cleaning in ethanol for a duration of 5 min. The test parameters for normal force, linear velocity, sliding path diameter and total sliding distance were configured as 50 N, 0.1 m/s, 12.5 mm and 1000 m, respectively. The tests were performed at room temperature in standard ambient conditions. Each sample was subjected to three ball-on-plate wear tests to improve statistical reproducibility.

2.6 Electrochemical analysis

Electrochemical tests were performed using a Princeton Applied Research multichannel potentiostat to investigate the corrosion resistance of the samples. The corrosion analyses were performed in a controlled environment at a

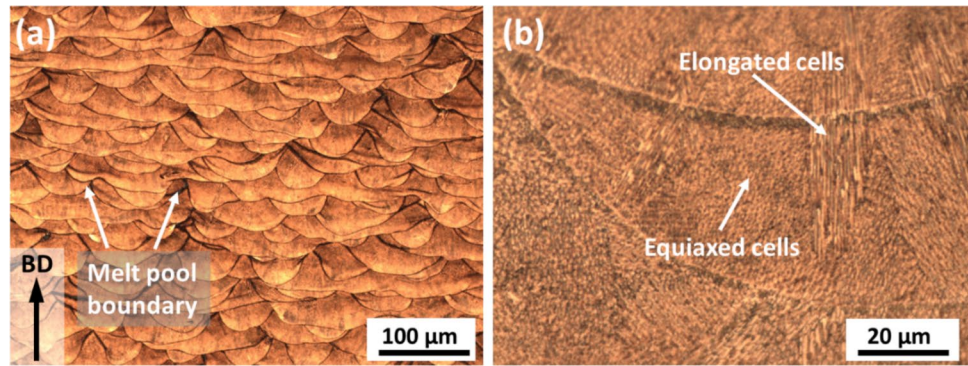
temperature of 25 ± 0.8 °C. The experimental setup consisted of a three-electrode system. The working electrode was made up of specimens with a surface area of 10 mm². The counter electrode was a platinum mesh, and the reference electrode was an Ag/AgCl-saturated KCl electrode with a potential of +0.197 V. A 3.5% NaCl solution (0.6 M NaCl) was used for all electrochemical tests. As part of the preparation process, each specimen was subjected to a pre-treatment process. This involved mechanical grinding with 4000 grit SiC sandpaper, followed by ultrasonic cleaning in acetone and ethanol for 5 min to ensure proper surface conditions. The assessment protocol commenced by measuring the open circuit potential (OCP) of each specimen for a duration of 1.5 h. Following that, electrochemical impedance spectroscopy (EIS) was performed, and the polarisation curves were recorded. EIS was conducted at the OCP, using a frequency range spanning from 100 kHz to 10 mHz. A sinusoidal perturbation signal with an amplitude of 10 mV was applied. The polarisation assessment was conducted by scanning the potential spectrum from -0.25 V to $+1.00$ V relative to the OCP at a scanning rate of 0.1667 mV/s. To guarantee the reproducibility, three duplicate experiments were carried out. Tafel plots were created to determine the corrosion potential (E_{corr}) and corrosion current density (I_{corr}) for each sample. Ultimately, the morphology of the corroded surfaces was examined using a Hitachi SU3500-A scanning electron microscope (SEM).

3 Results and discussion

3.1 Morphology of melt pools in the as-LPBF-fabricated 440C

Figure 2a presents the macrograph of the as-LPBF-fabricated 440C steel along the longitudinal cross-section, revealing the “fish-scale” melt pool patterns typically observed in LPBF-fabricated metals. It can be observed that the adjacent melt pools were partially overlapped without macroscopically perceivable cracks. This implies good bonding between the layers, consistent with the high density (99.98%) determined by the Archimedes method. A closer look at the individual melt pool reveals an ultrafine cellular structure as presented in Fig. 2b. This type of structure is associated with the high cooling rates ($\sim 10^6$ K/s) and the accompanied solute segregation upon LPBF process [6]. The cells can be observed as either equiaxed or elongated, depending on their growth directions, which are determined by the localised thermal gradients [34]. The apparent equiaxed cells are cross-sections of the elongated cells [35].

Fig. 2 Cross-sectional OM images of the as-LPBF-fabricated 440C illustrating **a** melt pools' morphology, **b** elongated and equiaxed cellular structures



3.2 Comparison between the as-LPBF-fabricated 440C and the wrought 440C

3.2.1 XRD phase analysis

The XRD spectra of the 440C powder, the as-LPBF-fabricated 440C and the HT wrought 440C specimens are presented in Fig. 3. Both the 440C powder and the as-LPBF-fabricated 440C predominantly exhibit face-centred cubic (FCC) austenite (γ -Fe) phase, with a minor presence of body-centred cubic (BCC) ferrite (α -Fe). The volume fractions of these two phases were found to be similar in both the 440C powder and the as-LPBF-fabricated 440C, as indicated by the quantitative phase analysis in Table 2. This similarity confirms that the high cooling rates during gas atomisation and the LPBF process did not facilitate the transformation of austenite into martensite, which is consistent with previous studies on the LPBF fabrication of AISI 440C [28–30]. In addition, the XRD diffractograms of these samples showed no evidence of carbide formation within the detection limits of the technique.

The absence of secondary carbides in the as-LPBF-fabricated steels has been previously attributed to the rapid heating and cooling rates inherent to the LPBF process, which prevents sufficient time for carbide formation, leaving carbide-forming elements as solutes in iron [7, 36]. Similarly, the 440C powder lacks carbides due to the high-temperature atomisation process (~ 1700 °C) followed by rapid cooling, which dissolves carbides and prevents their reformation [31, 37]. To further validate these observations, XRD analysis was also performed on samples fabricated using various processing parameters, and the results confirmed the absence of martensite and carbides regardless of cooling rates, as shown in Supplementary Fig. S.1.

In contrast, the XRD analysis of the HT wrought 440C reveals a distinct spectrum, characterised by the presence of martensite, $M_{23}C_6$ carbides and retained austenite phases typical for this alloy. According to the quantitative phase analysis in Table 2, the heat treatment of wrought 440C results in the transformation of 67.83% of austenite

into martensite, with 8.88 vol% of $M_{23}C_6$ carbides being formed.

3.2.2 Microstructure analysis

Building on the phase analysis obtained through XRD, further microstructural characterisation using EBSD and SEM–EDS was conducted to gain deeper insights into the microstructural morphology, phase distribution and elemental distribution within the as-LPBF-fabricated and the HT wrought 440C specimens. Before doing EBSD and EDS, all samples were carefully checked in the SEM, and no microcracks were observed. Figure 4a–d presents the EBSD-inverse pole figure (EBSD-IPF) maps and phase maps of the as-LPBF-fabricated and HT wrought 440C specimens. The IPF map of the as-LPBF-fabricated 440C (Fig. 4a) shows coarse columnar austenite grains with widths ranging from ~ 5 – 35 μm and lengths exceeding 100 μm . These columnar grains grew epitaxially from previous layers along the building direction (BD) during the LPBF process, spanning multiple layers. The IPF colour code indicates a random orientation of these columnar grains, without a preferential crystallographic texture. In addition, a small proportion of fine, equiaxed grains is interspersed amongst the columnar grains. The EBSD phase map of the as-LPBF-fabricated 440C (Fig. 4b) confirms a fully γ -austenite phase, with no BCC phase detected within the EBSD detection limit (step size of 0.1 μm). Furthermore, SEM images of the as-LPBF-fabricated 440C sample (Fig. 4e) reveal equiaxed and elongated cellular structures. EDS mapping indicates a uniform distribution of alloying elements across these structures, with darker regions primarily resulting from the “shadowing” effect, where the EDS detector could not collect signals from deeper areas within the sample [38, 39].

In contrast, the EBSD-IPF map of the HT wrought 440C specimen (Fig. 4c) demonstrates significant differences in microstructure, with much refined isotropic grains. The EBSD phase map in Fig. 4d reveals the non-uniform distribution of $M_{23}C_6$ carbides within the martensitic matrix carbides. Furthermore, a closer examination of the regions

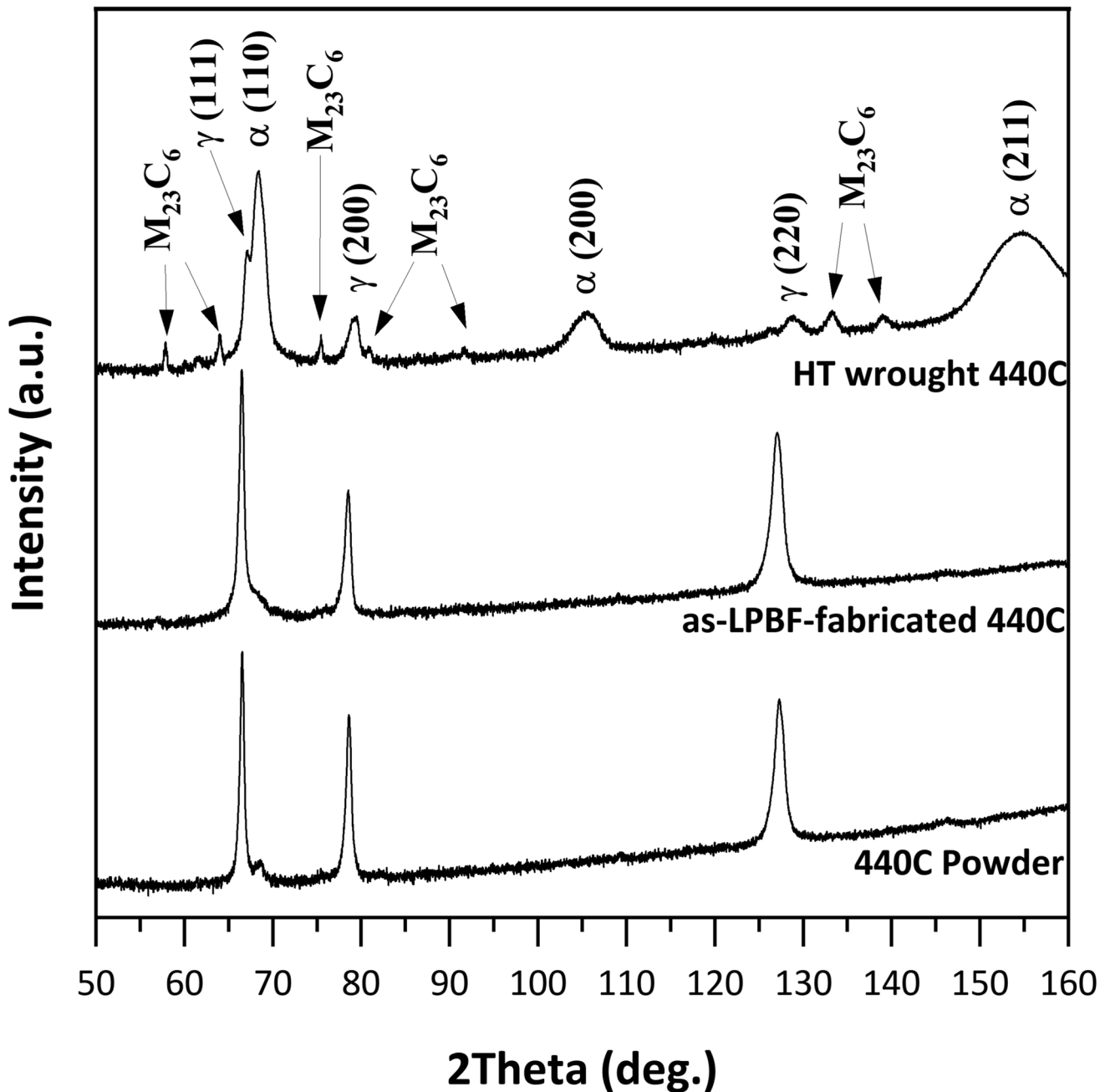


Fig. 3 X-ray diffraction spectra (Cr K_{α} radiation) of 440C powder, as-LPBF-fabricated 440C, and HT wrought 440C samples

Table 2 Quantitative phase analysis results in vol.%

Sample	FCC	BCC	$M_{23}C_6$
440C powder	96.95	3.05	0
As-LPBF-fabricated 440C	95.72	4.28	0
HT wrought 440C	23.29	67.83	8.88

surrounding the carbides reveals the presence of retained austenite as shown in the insert of Fig. 4d. This phenomenon is likely attributed to the chromium depletion caused by carbide formation, which reduces ferrite stabilisation in these regions. In addition, previous studies have demonstrated that the areas adjacent to these carbides exhibit localised nickel enrichment, which acts as an austenite stabiliser [40]. These combined effects create conditions for the retention of austenite. Furthermore, the SEM images of this sample (Fig. 4f) illustrate the presence of fine and coarse $M_{23}C_6$ carbides,

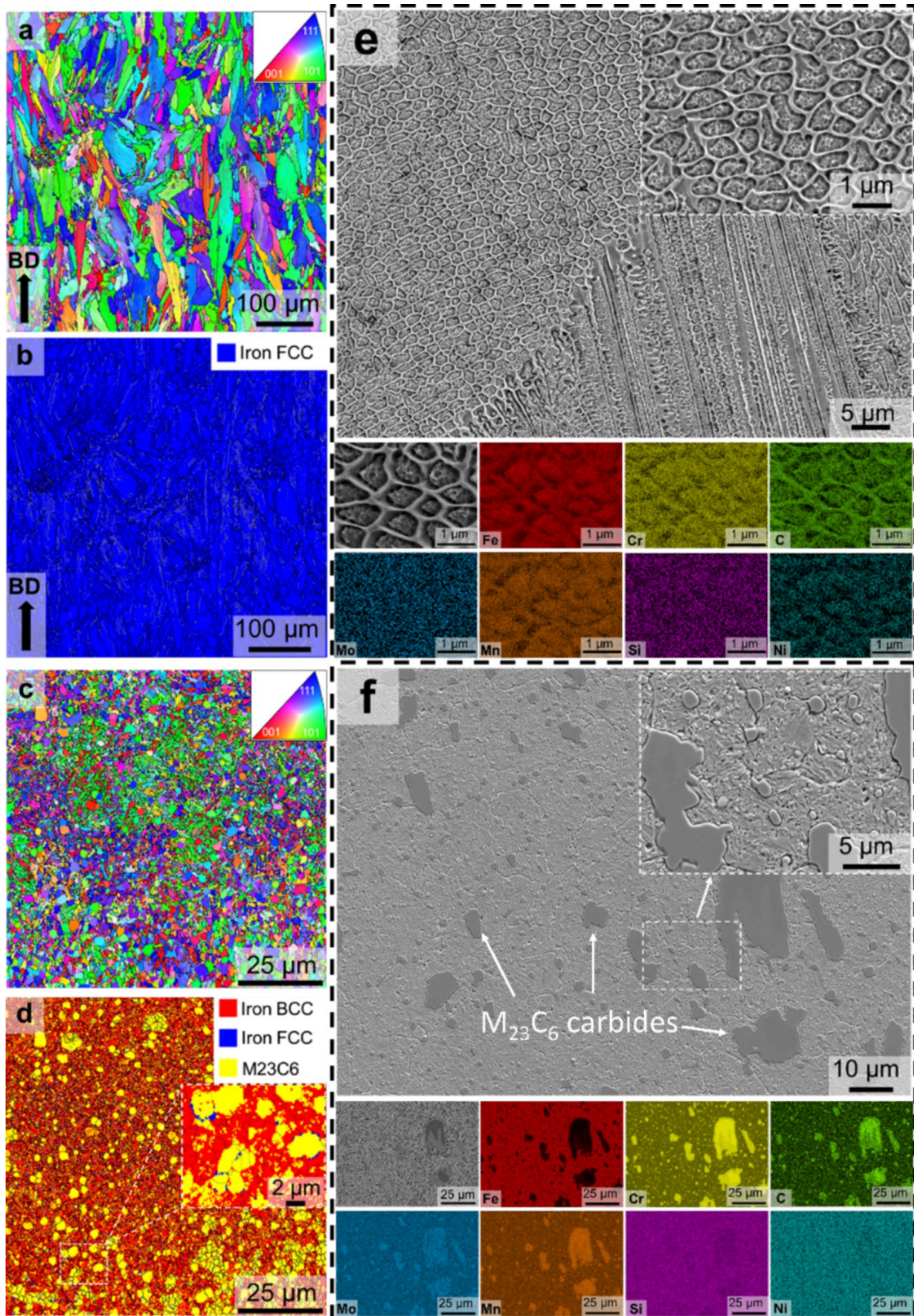


Fig. 4 EBSD-IPF map of **a**) as-LPBF-fabricated 440C, **c** HT wrought 440C with their corresponding EBSD phase maps (**b**, **d**). SEM images coupled with EDS maps of **e** as-LPBF-fabricated 440C and **f** HT wrought 440C

formed both along grain boundaries of the primary austenite and within the grains, reaching up to 18 μm in diameter with a high variability in size. These carbides are enriched with carbide-forming elements (C, Cr, Mo, and Mn) and depleted in iron, as confirmed by EDS analysis.

These findings highlight that, despite both samples undergoing high cooling rates during the LPBF process and quenching, their microstructure and phase compositions differ significantly. This underscores the necessity for a comprehensive investigation of the factors that are responsible for the absence of martensite in the as-LPBF-fabricated 440C, and to exploit potential solutions.

3.3 Factors affecting martensite transformation

The primary factors that influence martensitic transformation are the hardenability and the M_s of steels and the cooling rate. For a particular steel, the former two are relatively fixed; it needs to be cooled from the austenite phase field at a rate fast enough to prevent the decomposition of austenite into products such as ferrite and pearlite [4]. Studies have shown that the cooling rate during LPBF is adequate for martensite transformation in other LPBF-fabricated martensitic steels, including 420 and 431 stainless steels, and tool steels such as M2 [7, 41–43]. Therefore, given that the critical cooling rate necessary for martensitic transformation depends on factors such as the chemical composition of the steel, the cooling rate associated with LPBF can be deemed sufficient, ruling out the cooling rate as the cause for the absence of martensite in the as-LPBF-fabricated 440C samples.

However, the M_s temperature, which indicates the thermodynamic driving force required to initiate the transformation of austenite into martensite, is primarily governed by the chemical composition of the steels [4, 33, 44]. Various empirical equations have been developed to estimate the M_s temperature based on the nominal chemical composition of steels. For high-alloy steels, the following equation is often applied [45]:

$$M_s(^{\circ}\text{C}, \text{wt.}\%) = 550 - 350C - 40Mn - 20Cr - 10Mo - 17Ni - 8W - 35V - 10Cu + 15Co + 30Al \quad (1)$$

According to the applied empirical equation, all alloying elements, except cobalt and aluminium, decrease the M_s temperature, with carbon exerting the most pronounced effect. Nitrogen is also known to influence the M_s temperature; however, it was not considered in the present analysis because the LPBF processing was conducted under an argon atmosphere, and the nitrogen content of the nitrogen-atomized powder was not specified in the chemical composition provided by the supplier. Based on this equation, the

M_s temperature of the AISI 440C alloy was estimated to be approximately 150.2 $^{\circ}\text{C}$ below zero.

This subzero M_s temperature suggests that martensite transformation in the AISI 440C alloy cannot occur during the LPBF processing, regardless of the cooling rate and other factors that can suppress thermally induced martensitic transformation, such as the presence of cellular structures in the additively manufactured steels, as reported previously [46].

Therefore, to validate this hypothesis and promote martensite formation, deep cryogenic treatment (DCT) was employed on the LPBF-fabricated 440C. DCT is typically used to reduce retained austenite in high-alloy steels, which generally exhibit low M_s temperatures [47–49]. The effectiveness of the austenite-to-martensite transformation following DCT depends on whether the martensite finish temperature (M_f) is above or below the DCT temperature.

In addition, the heat treatment process traditionally used for wrought 440C was applied to the LPBF-fabricated 440C. This was to assess whether carbide formation inherent in this process could raise the M_s temperature of the as-LPBF-fabricated samples. This would provide insights into whether conventional heat treatment could enhance the mechanical properties of LPBF-fabricated 440C by promoting austenite-to-martensite transformation.

3.4 Post-processing treatment on LPBF-fabricated 440C

3.4.1 XRD phase analysis

XRD spectra of the DCT LPBF-fabricated and HT LPBF-fabricated 440C specimens are shown in Fig. 5. The absence of martensite peaks and the presence of only austenite peaks indicate that the cryogenic treatment did not facilitate the transformation of austenite into martensite. Consequently, the phase constituent (Table 3), consisting of γ -Fe and α -Fe phases, remained nearly identical to that observed in the as-LPBF-fabricated 440C sample, as

detailed in Table 2. This outcome suggests that the actual M_s temperature of the LPBF alloy is likely lower than the boiling point of liquid nitrogen (-196°C), despite the calculated M_s temperature being -150.2°C . Discrepancies between calculated M_s temperatures and experimentally measured values have been documented in the literature and are often attributed to the non-linear relationship between M_s temperature and solute concentrations, particularly in highly alloyed steels [45, 50]. This non-linearity can lead to significant deviations in M_s predictions,

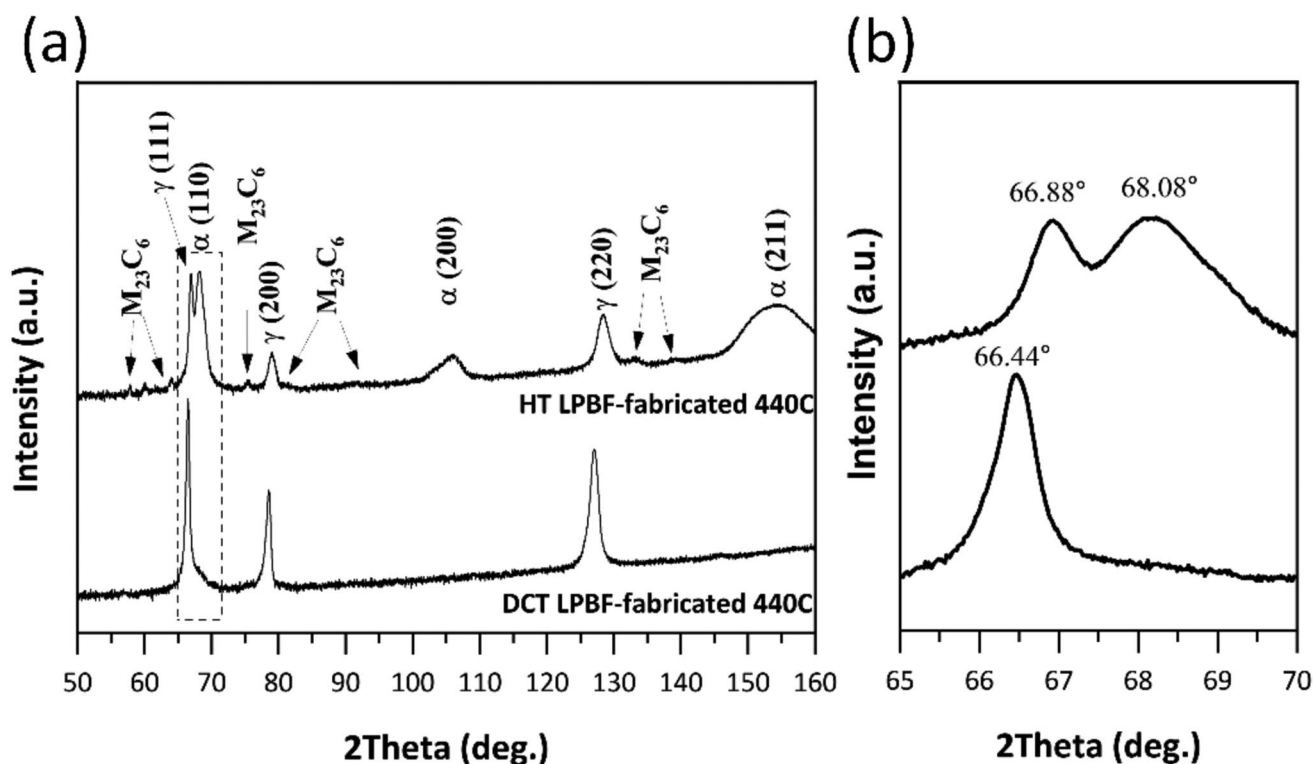


Fig. 5 **a** X-ray diffraction spectra (Cr K α radiation) of DCT LPBF-fabricated 440C and HT LPBF-fabricated 440C samples; **b** magnified spectra detailing positions of (111) γ and (110) α peaks

Table 3 Quantitative phase analysis results in vol.%

Sample	FCC	BCC	M ₂₃ C ₆
DCT LPBF-fabricated 440C	95.87	4.13	0
HT LPBF-fabricated 440C	38.45	53.18	8.37

especially when complex interactions between multiple alloying elements are involved.

Unlike the DCT, XRD analysis of the HT LPBF-fabricated sample identified the presence of martensite, M₂₃C₆ carbides, and retained austenite. Notably, the magnified spectra in Fig. 5b shows a shift of the primary (111) γ peak from 66.44° towards higher angle of 66.88°, indicating the reduction in carbon content in the austenite because the formation of carbides depleted alloying elements such as chromium and carbon from the austenite, leading to a reduction in lattice parameters and contributing to the peak shift [51, 52]. Quantitative phase analysis, as shown in Table 3, reveals that whilst the volume fraction of M₂₃C₆ carbides in the HT LPBF-fabricated 440C is comparable to that in the HT wrought 440C, the HT LPBF-fabricated 440C exhibits a higher retained austenite content (38.45%) compared to its wrought counterpart (23.29%).

3.4.2 Microstructure analysis

The EBSD-IPF and phase maps of the DCT LPBF-fabricated and HT LPBF-fabricated samples are presented in Fig. 6. The DCT LPBF-fabricated sample (Fig. 6a) displays columnar austenite grains that are identical in size and orientation to those observed in the as-LPBF-fabricated 440C, indicating no alteration in grain structure or crystallographic texture following cryogenic treatment. The EBSD phase map (Fig. 6b) further confirms the single presence of the γ -Fe phase, with no evidence of martensitic transformation. These observations, along with the XRD analysis, strongly suggest that the DCT process did not induce the martensitic transformation in the sample. However, as highlighted in previous studies [26, 47, 48, 53, 54], the DCT process may influence the residual stresses inherent to the LPBF process, and therefore affect the material properties. This will be further investigated in the subsequent sections.

In contrast, HT LPBF-fabricated 440C samples demonstrate significant differences in microstructure, regarding grain size and morphology evidenced in its IPF map in Fig. 6c. Combining these results with the EBSD phase map in Fig. 6d, the formation of M₂₃C₆ carbides and martensite resulted in a significant refinement of the overall microstructure, with fine M₂₃C₆ carbides distributed in the matrix of martensite. Comparing the EBSD results of HT

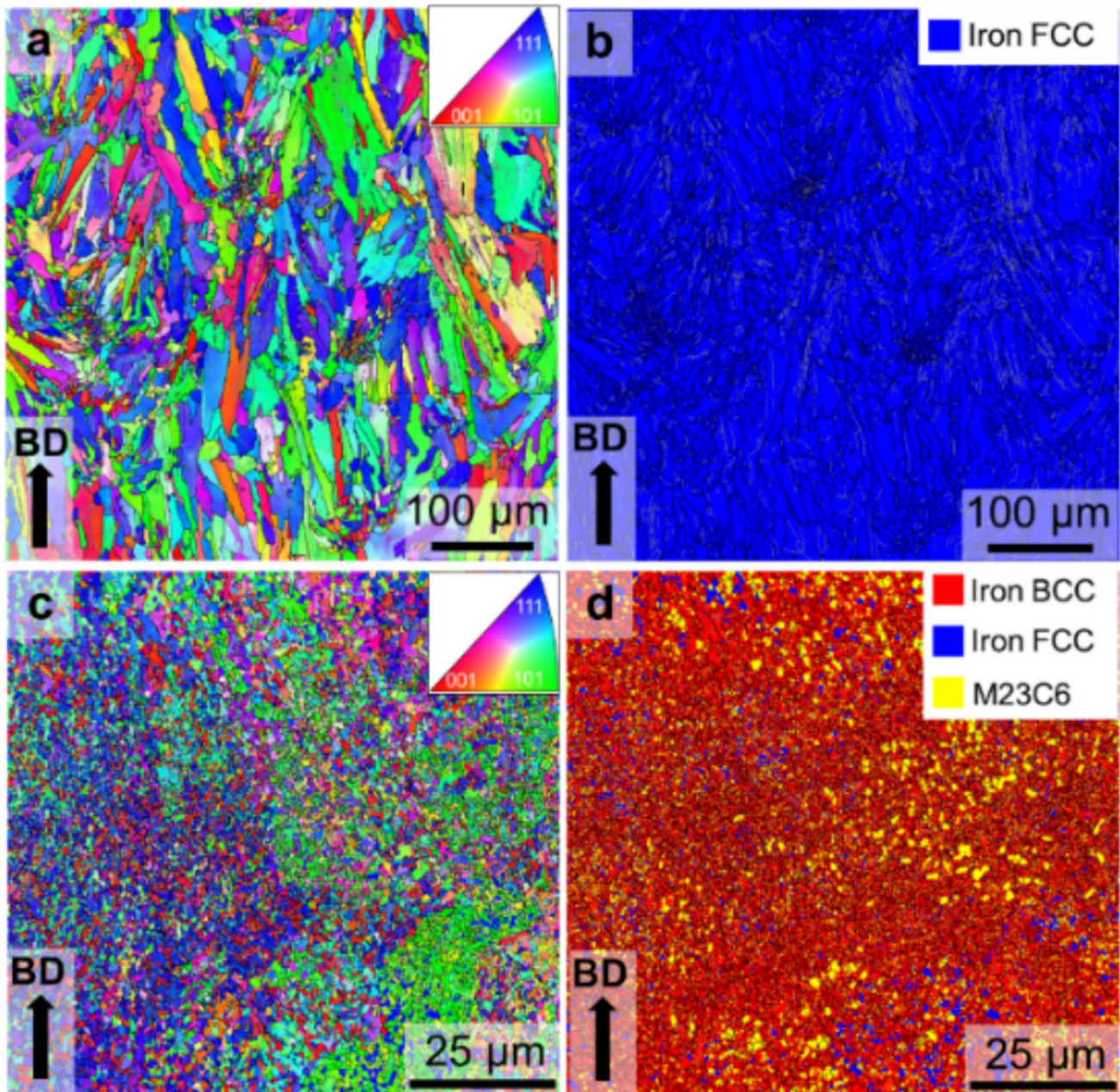


Fig. 6 EBSD-IPF map of **a** DCT LPBF-fabricated 440C, **c** HT LPBF-fabricated 440C with their corresponding EBSD phase maps (**b**, **d**)

LPBF-fabricated 440C with the HT wrought 440C, it is evident that the HT LPBF-fabricated 440C has a much finer microstructure with much smaller $M_{23}C_6$ carbide particles. In addition, the distribution of $M_{23}C_6$ carbides is more uniform in the HT LPBF-fabricated 440C compared to the HT wrought 440C sample. The observed differences in grain size and $M_{23}C_6$ carbide size explain the higher fraction of retained austenite in the heat-treated (HT) LPBF-fabricated 440C compared to the HT wrought counterpart. This is because finer carbides are associated with a higher interfacial area, creating more chromium-depleted and Ni-enriched

regions adjacent to these carbides, which promotes austenite retention. Thus, despite identical heat treatment sequences and the same volume percentage of carbides, the finer $M_{23}C_6$ carbides in the HT LPBF-fabricated 440C sample result in more retained austenite.

SEM images of the HT LPBF-fabricated 440C sample (Fig. 7) also illustrate the presence of fine $M_{23}C_6$ carbides, which formed both at the grain boundaries of the primary austenite and within the grains themselves, with sizes below $2\mu\text{m}$ and less variability in size compared to the wrought 440C. EDS maps confirm that these carbides are enriched

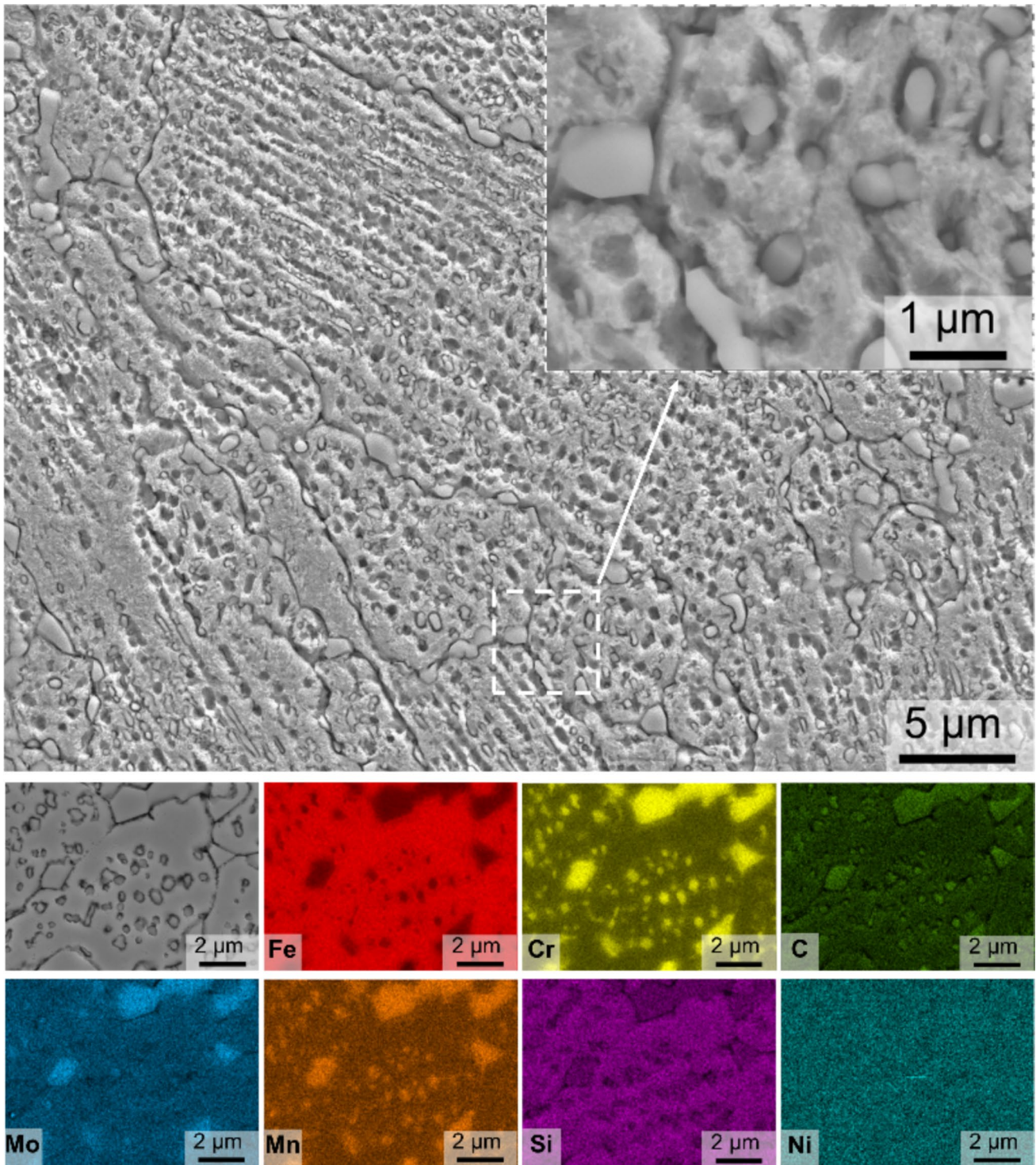


Fig. 7 SEM images of HT LPBF-fabricated 440C coupled with EDS maps

with carbide-forming elements whilst being depleted in iron. This is the same as in the wrought 440C.

Based on the phase analysis of the samples, it is evident that carbide formation in AISI 440C plays a critical role in enabling the formation of martensite. Although XRD

and SEM analyses did not detect carbides in the as-LPBF-fabricated samples, the possibility of nano-sized carbides cannot be ruled out, as noted in previous studies on LPBF-processed 440C [30].

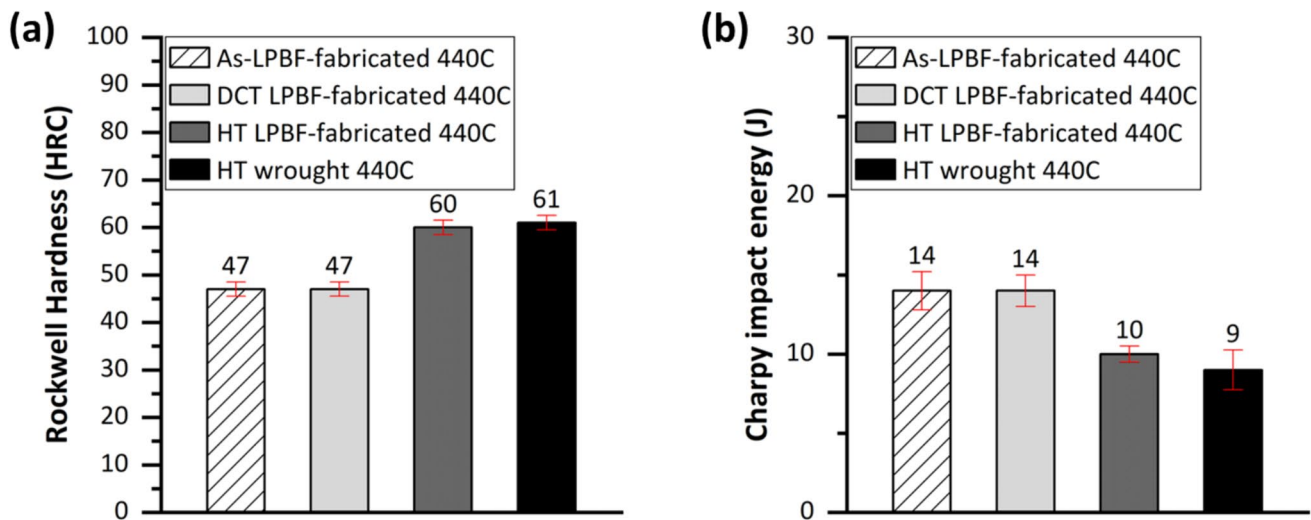


Fig. 8 a Rockwell hardness results of samples under a load of 150kgf. b Charpy impact test results

Carbide formation depletes key alloying elements such as carbon and chromium from the austenite matrix, which in turn raises the M_s temperature, facilitating the transformation of austenite into martensite [20, 55]. Compared to other martensitic stainless steels such as 420 and 431, the 440C steel has higher alloying content, which lowers the M_s temperatures below room temperature. Hence, post-heat treatment becomes essential for this alloy, either LPBF-fabricated or wrought, to induce martensitic transformation, achieving the desired mechanical properties.

3.5 Mechanical properties evaluation

Figure 8a presents the Rockwell hardness of the 440C samples. Both the as-LPBF-fabricated and DCT 440C exhibit a relatively low hardness of 47 ± 1.3 HRC, primarily due to the dominant presence of the soft austenitic phase. This value is higher than the previously reported 39 HRC for additively fabricated 440C [28]. This can be attributed to factors such as the relative density of the samples, grain size, and texture of the microstructure resulting from different LPBF process parameters. However, the microstructure of LPBF-fabricated 440C has not been extensively studied before, limiting direct comparisons and conclusions. In addition, the cryogenically treated sample displayed the same hardness value, corroborating the XRD and EBSD analyses, which indicated no phase transformation due to cryogenic treatment. Furthermore, the potential changes in residual stress after DCT did not affect the hardness.

A significant increase in hardness to 60 ± 1.8 HRC was observed after the heat treatment of the LPBF-fabricated 440C as a result of the martensitic transformation and the formation of $M_{23}C_6$ carbides in the sample. Remarkably, the hardness value is comparable to that of the HT wrought

440C with a hardness of 61 ± 1.9 HRC. Although the HT LPBF-fabricated sample contains a higher volume fraction of retained austenite (38.45 vol.%) than the HT wrought counterpart (23.29 vol.%), the finer and well-dispersed carbide particles and much finer grains in the HT LPBF-fabricated 440C complement the hardness. This indicates that appropriate heat treatment is necessary for the LPBF-fabricated 440C stainless steel to achieve a hardness that is comparable to its conventionally fabricated counterpart.

The Charpy impact test results are presented in Fig. 8b. Both the as-LPBF-fabricated and DCT LPBF-fabricated 440C samples exhibit a Charpy impact energy of approximately 14 J, indicating higher toughness compared to the HT LPBF-fabricated and HT wrought 440C samples, which recorded impact energies of 10 J and 9 J, respectively. This higher impact toughness is attributed to the predominant austenitic phase in these samples before heat treatment. In addition, the close impact energies suggest that the potential changes in residual stress after DCT do not affect the toughness. The lower Charpy impact energies of both the HT LPBF-fabricated and wrought 440C samples are obviously due to the formation of hard martensite and $M_{23}C_6$ carbides. But the Charpy impact energy of the HT LPBF-fabricated sample is slightly higher than the wrought counterpart, which is attributed to its higher volume fraction of retained austenite. The measured Charpy impact energy of the heat-treated samples in this study is approximately 2 J higher than the previously reported value [22]. This could be due to the higher austenitization temperatures used in other studies, leading to the formation of both M_7C_3 and $M_{23}C_6$ carbides [22–24]. M_7C_3 carbides typically form as coarse, semicontinuous networks along the primary austenite grain boundaries, facilitating crack propagation, thereby reducing ductility and toughness [22].

Fig. 9 Engineering tensile stress–strain curves for LPBF-fabricated samples in both longitudinal and transverse directions, and HT wrought 440C

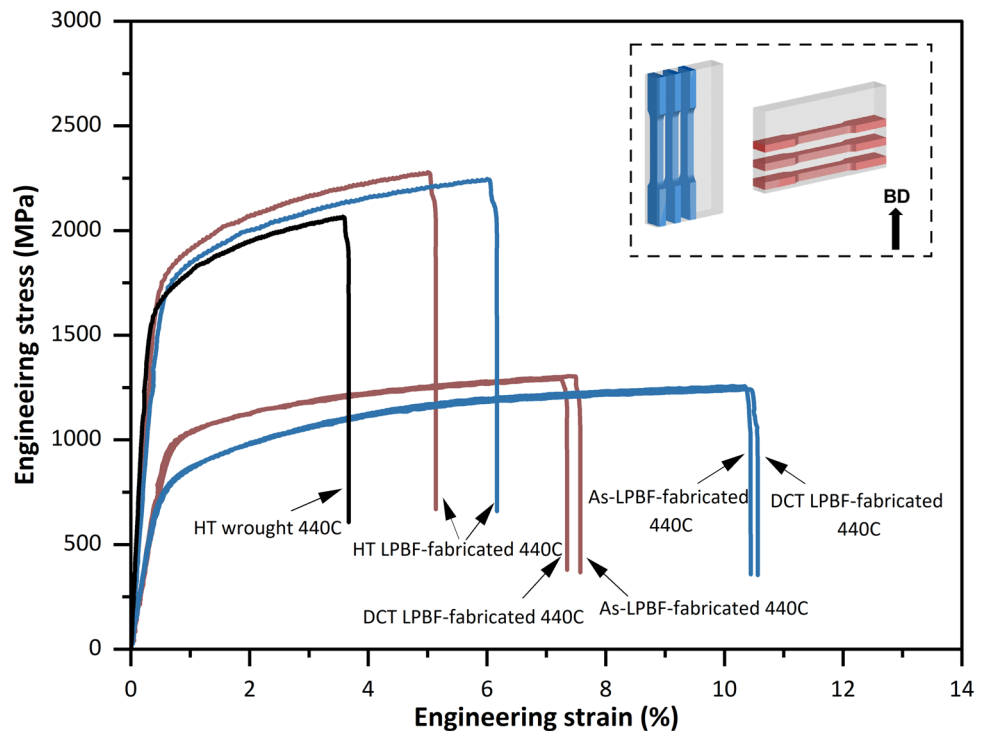


Table 4 Yield strength (YS), ultimate tensile strength (UTS) and elongation to failure (EL)

Sample	Direction to BD	YS (MPa)	UTS (MPa)	EL (%)
As-LPBF-fabricated 440C	Longitudinal	711 ± 6	1254 ± 3	10.3 ± 0.6
	Transverse	966 ± 5	1303 ± 4	7.3 ± 1.2
DCT LPBF-fabricated 440C	Longitudinal	720 ± 9	1246 ± 8	10.1 ± 1.3
	Transverse	968 ± 2	1293 ± 6	7.6 ± 1.2
HT LPBF-fabricated 440C	Longitudinal	1691 ± 3	2235 ± 5	6.1 ± 1.1
	Transverse	1724 ± 7	2273 ± 4	5.1 ± 0.7
HT Wrought 440C	N/A	1567 ± 6	2069 ± 3	3.7 ± 0.4

Figure 9 illustrates the engineering tensile stress–strain curves for LPBF-fabricated samples in both longitudinal and transverse directions, and HT wrought 440C. The yield strength (YS), ultimate tensile strength (UTS) and elongation to failure (EL) are detailed in Table 4. The as-LPBF-fabricated 440C steel exhibits significant anisotropy in its tensile properties, with higher YS (966 ± 5 MPa) and UTS (1303 ± 4 MPa) but lower EL ($7.3\% \pm 1.2\%$) along the transverse direction compared to the YS (711 ± 6 MPa), UTS (1254 ± 3 MPa) and EL ($10.3\% \pm 0.6\%$) along the longitudinal direction. This anisotropy is attributed to the elongated austenite grains aligned with the building direction, as confirmed by EBSD-IPF maps. This result differs from previously reported properties of LPBF austenitic stainless steels, which showed higher strength and lower ductility along the transverse direction than the longitudinal direction due to the weak interlayer [11, 56]. In addition, the DCT does not change the tensile properties of the LPBF-fabricated samples

in both directions, which is consistent with the microstructural examination.

Post-heat treatment led to substantial improvement in tensile properties and lower anisotropy of the LPBF-fabricated 440C steel due to the formation of martensite and $M_{23}C_6$ carbides, which not only strengthen the steel but also weaken the preferred crystallographic orientations. The HT LPBF-fabricated samples demonstrate a YS of 1724 ± 7 MPa and UTS of 2273 ± 4 MPa along the transverse direction, and a YS of 1691 ± 3 MPa and UTS of 2235 ± 5 MPa along the longitudinal direction. However, the elongation was reduced to $5.1\% \pm 0.4\%$ and $6.1\% \pm 0.6\%$ for the transverse and longitudinal directions, respectively. The elimination of columnar grains through the formation of martensite and carbides in the heat-treated samples resulted in lower anisotropy in tensile properties compared to the as-LPBF-fabricated and DCT LPBF-fabricated samples. The remaining anisotropy can be attributed to the weakening of the interlayer

boundaries as reported in austenitic stainless steels [11, 56]. More importantly, the HT LPBF-fabricated sample exhibited significantly superior tensile properties compared to the HT wrought 440C, which has an YS of 1567 ± 6 MPa, UTS of

2069 ± 3 MPa and EL of $3.7\% \pm 0.4\%$. This superior performance of the HT LPBF-fabricated 440C can be attributed to several factors. First, the more homogeneously distributed and finer $M_{23}C_6$ carbides in the HT LPBF-fabricated

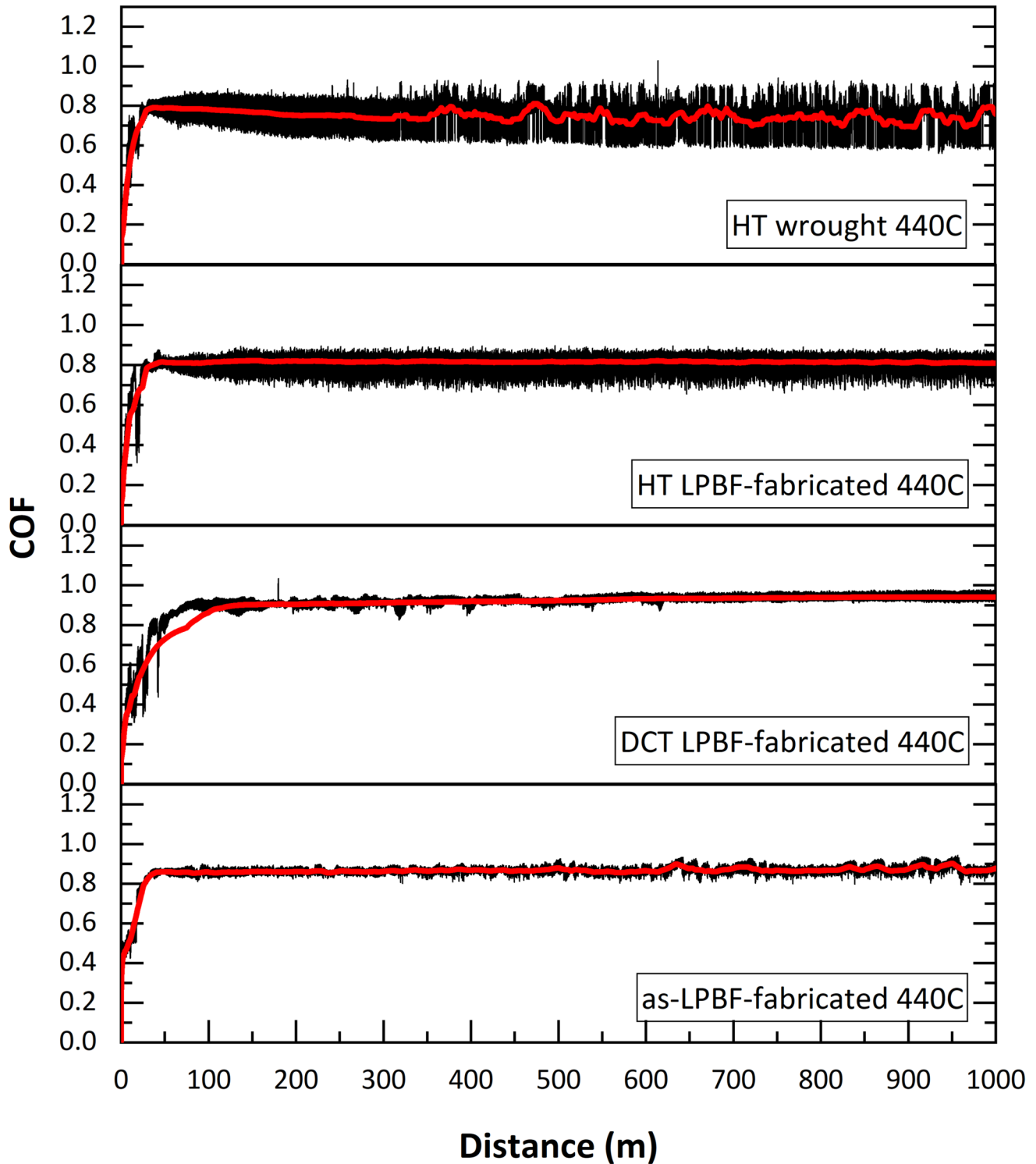


Fig. 10 Variation of COF along the sliding distance of the samples

sample act as more effective obstacles to dislocation movement, thereby enhancing YS and UTS. Second, the refined grains of the HT LPBF-fabricated 440C contribute to the Hall–Petch strengthening mechanism. In addition, the higher retained austenite content in the HT LPBF-fabricated 440C improved ductility. Therefore, the combined effects of these factors result in superior tensile properties of the HT LPBF-fabricated 440C compared to its wrought counterpart.

3.6 Wear resistance

As a high-carbon steel, 440C is commonly used to make bearings, knife blades and other tools. Hence, it is essential to evaluate the wear behaviour of the LPBF-fabricated steel. Figure 10 presents the coefficient of friction (COF) of various 440C samples versus sliding distance tested at a load of 50 N with a total travel distance of 1000 m. In this figure, the black curves indicate the minimum and maximum COF, whilst the red curves represent the mean COF. The average COF values and the specific wear rates of each sample are detailed in Table 5. The specific wear rate was calculated by dividing the mean volume losses (mm^3) by the total sliding distance (m) and the normal force (N) applied during the test [57, 58].

The wear test results indicate that both the as-LPBF-fabricated 440C and the DCT LPBF-fabricated 440C samples exhibited stable COF values, demonstrating consistent frictional performance with COF values of 0.86 and 0.87, respectively. Their specific wear rates were also relatively similar, measured at $12.64 \pm 0.37 \times 10^{-7} \text{ mm}^3/\text{Nm}$ and $12.43 \pm 0.33 \times 10^{-7} \text{ mm}^3/\text{Nm}$, respectively. However, after heat treatment, the wear performance of the LPBF-fabricated samples showed substantial improvement, with a reduced COF of 0.81 and a lower specific wear rate of $3.32 \pm 0.42 \times 10^{-7} \text{ mm}^3/\text{Nm}$. This enhancement in wear performance is attributed to the formation of hard phases, such as martensite and carbides, in contrast to the predominantly austenitic phase present in the as-LPBF-fabricated and DCT LPBF-fabricated 440C samples. The presence of these hard phases results in less degradation of the surface when in contact with the YSZ ball used in this study.

The observed fluctuations in the COF of the heat-treated LPBF-fabricated sample during the test can be attributed to the surface roughness caused by the presence of carbides. When comparing the wear performance of the HT

LPBF-fabricated 440C with the HT wrought 440C, it is evident that the HT LPBF-fabricated 440C, with its finer and more uniformly distributed carbides and consequently lower surface roughness, demonstrates a more stable COF during wear testing. The uniformity in carbide distribution ensures a consistent wear surface, reducing fluctuations in frictional forces and providing more stable wear performance.

In addition, the HT wrought 440C exhibited a higher wear rate of $4.82 \pm 1.2 \times 10^{-7} \text{ mm}^3/\text{Nm}$, which can be attributed to its coarser microstructure and the non-uniform distribution of coarse carbides. The higher retained austenite content in the HT LPBF-fabricated 440C also contributes to its improved wear performance by absorbing and redistributing stress during wear, thus preventing premature carbide pull-out or micro-cracking, which can lead to increased wear resistance.

3.7 Electrochemical analysis

As a typical stainless steel, the corrosion behaviour of the LPBF-fabricated 440C is a common concern. Figure 11a presents the potentiodynamic polarisation (PDP) curves for samples tested in 3.5 wt.% NaCl solution at room temperature. Both the as-LPBF-fabricated 440C and DCT LPBF-fabricated 440C samples exhibit typical passive behaviour, as evidenced by the formation of effective passivation layers on their surfaces at a constant current density. This behaviour is attributed to the primary austenite phase in both samples and the uniform distribution of chromium within the microstructure, promoting the formation of a protective Cr_2O_3 oxide layer that enhances passivation. As listed in Table 6, the corrosion potential (E_{corr}) and corrosion current density (I_{corr}) derived from the PDP curves are $-0.13 \pm 0.06 \text{ V}$ and $-0.14 \pm 0.09 \text{ V}$, and $4.91 \times 10^{-8} \text{ A/cm}^2$ and $5.05 \times 10^{-8} \text{ A/cm}^2$, for the as-LPBF-fabricated 440C and DCT LPBF-fabricated 440C samples, respectively. These marginal differences are results of the same microstructure in both samples.

The HT LPBF-fabricated 440C and HT wrought 440C samples demonstrate lower E_{corr} values of $-0.19 \pm 0.08 \text{ V}$ and $-0.23 \pm 0.06 \text{ V}$, respectively, indicating a higher thermodynamic tendency towards corrosion in the 3.5 wt.% NaCl solution. In addition, these samples exhibit significantly higher I_{corr} values and, consequently, higher corrosion rates compared to the as-LPBF-fabricated and DCT

Table 5 Average COF and specific wear rates of samples

Sample	Average COF	Specific wear rate (mm^3/Nm)
As-LPBF-fabricated 440C	0.86	$12.64 \pm 0.37 \times 10^{-7}$
DCT LPBF-fabricated 440C	0.87	$12.43 \pm 0.33 \times 10^{-7}$
HT LPBF-fabricated 440C	0.81	$3.32 \pm 0.42 \times 10^{-7}$
HT Wrought 440C	0.84	$4.82 \pm 1.2 \times 10^{-7}$

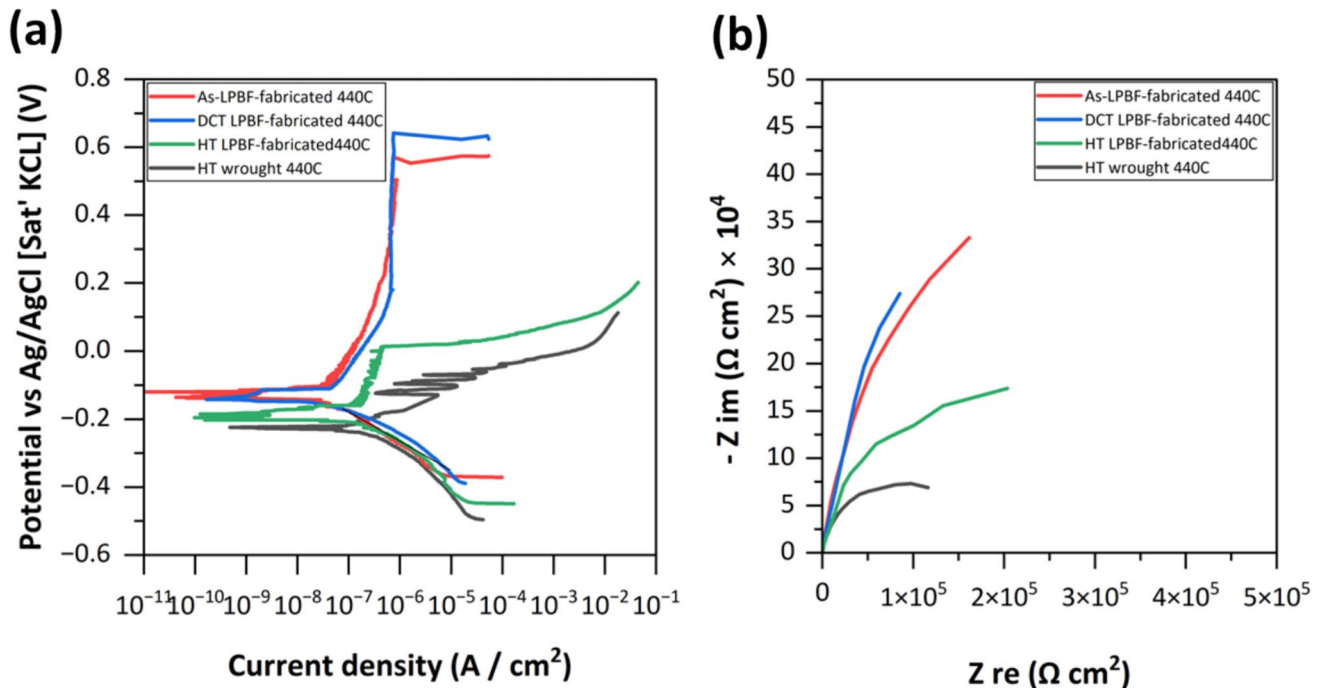


Fig. 11 **a** Potentiodynamic polarisation curves for samples tested in 3.5 wt.% NaCl. **b** Nyquist plots of samples

Table 6 Corrosion potential (E_{corr}) and corrosion current (I_{corr}) of the samples

Sample	E_{corr} (V)	I_{corr} (A/cm ²)
As-LPBF-fabricated 440C	-0.13 ± 0.06	4.91×10^{-8}
DCT LPBF-fabricated 440C	-0.14 ± 0.09	5.05×10^{-8}
HT LPBF-fabricated 440C	-0.19 ± 0.08	1.45×10^{-7}
HT Wrought 440C	-0.23 ± 0.06	7.91×10^{-7}

LPBF-fabricated 440C samples. This increase in corrosion rate is attributed to the transformation of the more corrosion-resistant austenite phase into martensite, as well as the formation of $M_{23}C_6$ carbides. The body-centred tetragonal (BCT) structure of martensite is more susceptible to corrosion due to its higher density of dislocations and residual stresses, which serve as sites for corrosion initiation and pitting [59]. Moreover, the presence of carbides can create galvanic cells that accelerate galvanic corrosion and hinder the regeneration of the passive film in martensitic stainless steels [60]. The formation of chromium-rich carbides also leads to chromium-depleted zones in the matrix, which typically act as preferential sites for pitting corrosion, resulting in faster material degradation [59, 60].

However, from Fig. 11 and Table 6, it can be seen that the HT LPBF-fabricated 440C exhibits higher corrosion resistance than the HT wrought 440C. Following two factors are responsible for such enhancement. First, the higher

retained austenite fraction in the HT LPBF-fabricated 440C (38.45 vol.%) compared to the HT wrought 440C (23.29 vol.%) contributes to lowering the corrosion propagation, as retained austenite has been shown to positively affect corrosion resistance in other martensitic stainless steels, such as super 13Cr [40]. Second, whilst the volume fraction of $M_{23}C_6$ carbides remains the same in both samples, the finer and more uniformly distributed carbides in the HT LPBF-fabricated 440C reduce the galvanic effect between carbides and the matrix, enhancing corrosion resistance.

The Nyquist plots (Fig. 11b) illustrate capacitive arc characteristics for all samples, reflecting their passive film stability and resistance to electrochemical dissolution. In these plots, a larger semicircular diameter indicates greater resistance to electrochemical dissolution and higher passive film stability. The diameters of the capacitive plots for the HT LPBF-fabricated 440C and HT wrought 440C samples are smaller than those for the as-LPBF-fabricated and DCT LPBF-fabricated 440C samples, which have relatively similar diameters. In addition, the HT wrought 440C exhibits a smaller diameter than the HT LPBF-fabricated 440C, indicating inferior protection provided by the passive film on the former.

SEM images of the surfaces of the HT LPBF-fabricated and HT wrought 440C samples after corrosion testing (Fig. 12) further confirm these findings. The HT wrought 440C sample shows significantly larger, deeper, and more severe corrosion attacks compared to the HT

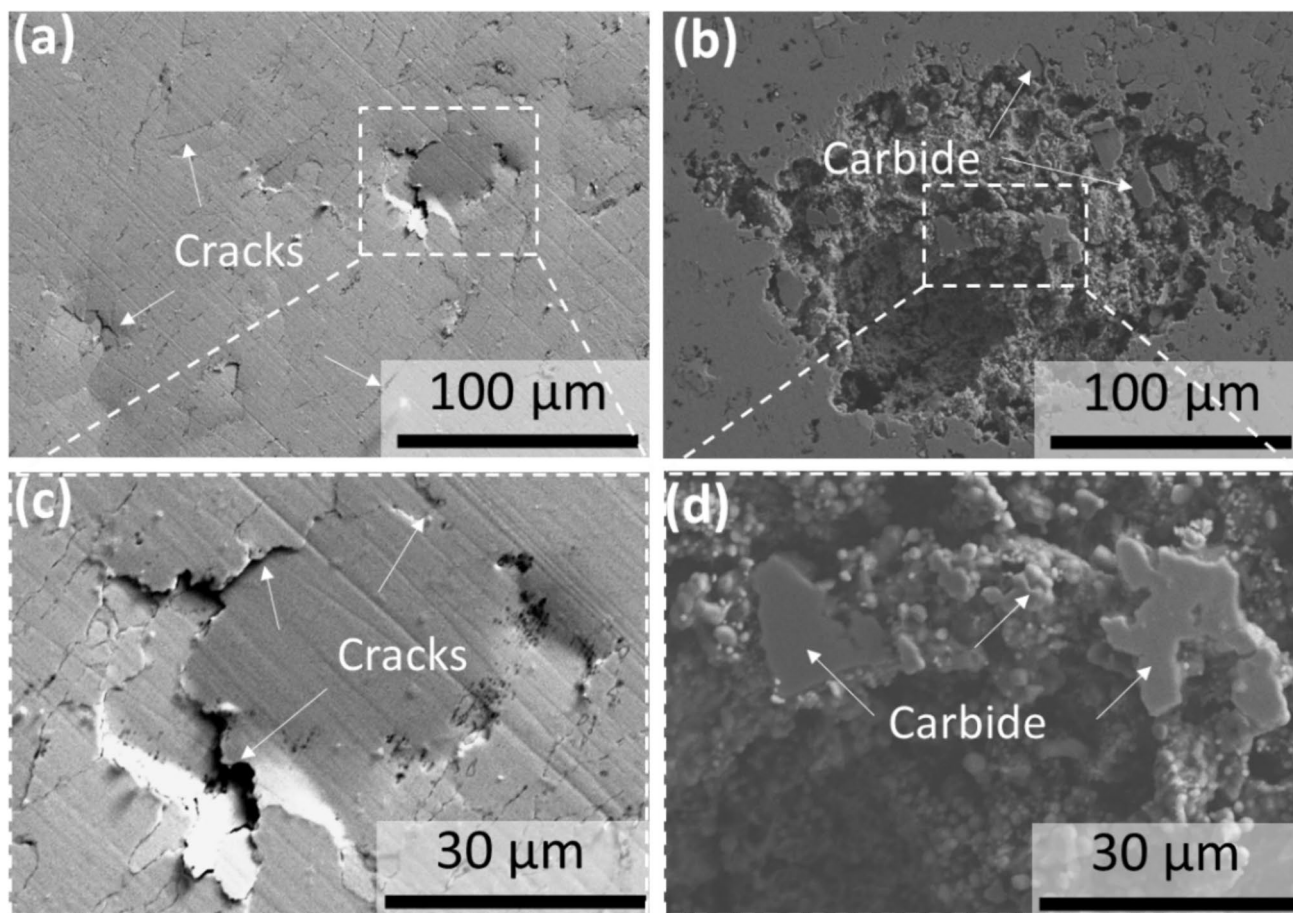


Fig. 12 SEM images of the surface of HT LPBF-fabricated (a, c) and HT wrought 440C (b, d) samples after corrosion testing

LPBF-fabricated 440C sample. This visual evidence aligns with the quantitative electrochemical data, conclusively demonstrating the enhanced corrosion resistance of HT LPBF-fabricated 440C stainless steel compared to its wrought counterpart. This superior performance highlights the potential of additive manufacturing to produce AISI 440C components with improved corrosion resistance, offering a compelling advantage over traditional manufacturing techniques.

The findings of this study are consistent with previous reports regarding the absence of martensite in as-LPBF-fabricated 440C steel and its associated undesirable properties [28–30]. However, this work presents a systematic investigation into the mechanisms underlying the absence of martensite, which has not been explored previously. The results reveal that a high solute concentration in the austenite parent phase leads to a significantly reduced M_s temperature, without the formation of a substantial amount of carbides, as observed in wrought samples following heat treatment. These findings underscore the critical importance of applying a full heat treatment to LPBF-fabricated 440C steel to promote martensitic

transformation and achieve desirable properties. Looking ahead, compositional modifications aimed at reducing the solute content in austenite and increasing the M_s temperature may provide a more efficient pathway to martensitic transformation, thereby minimising the need for extensive post-processing.

4 Conclusion

This study investigated the LPBF fabrication of the AISI 440C steel, emphasising processability, microstructural evolution, heat treatment response and performance comparison with wrought 440C steel. The main findings are:

- The AISI 440C exhibits high LPBF processability, achieving a relative density of > 99.98%. However, the as-built microstructure remains fully austenitic due to a suppressed martensitic transformation resulting from the low M_s temperature and cellular structure of the LPBF-fabricated alloy.

- Heat treatment facilitates martensitic transformation via fine $M_{23}C_6$ carbide precipitation, which increases the M_s temperature.
- Both LPBF and wrought samples show similar carbide fractions after heat treatment, but LPBF steel retains more austenite due to finer grains and localised stabilisation.
- As-built samples exhibit ~41 HRC hardness and 14 J impact energy; after treatment, both variants reach ~60 HRC, with LPBF steel offering enhanced toughness due to the retained austenite.
- Tensile strength in the as-built condition is limited but shows anisotropy (UTS up to 1303 ± 4 MPa). Post-treatment not only eliminated the property anisotropy, but also significantly improved strength (YS: 1724 ± 7 MPa, UTS: 2273 ± 4 MPa) and ductility (elongation: $6.1 \pm 1.1\%$), exceeding the performance of heat-treated wrought 440C steel.
- Heat-treated LPBF 440C achieves the lowest wear rate ($4.82 \pm 1.2 \times 10^{-7}$ mm³/Nm) due to finer microstructure and stress-absorbing retained austenite.
- As-built samples exhibit strong passivation behaviour. Whilst corrosion resistance decreases after post-treatment, LPBF samples still outperform the wrought samples due to finer carbides and higher retained austenite.

These findings demonstrate that LPBF, combined with an optimised heat treatment, enables the AISI 440C steel to achieve superior mechanical properties, wear and corrosion resistance for demanding applications.

Supplementary Information The online version contains supplementary material available at <https://doi.org/10.1007/s40964-025-01294-z>.

Acknowledgements The authors thank Australian Microscopy & Microanalysis Research Facility at the Centre for Microscopy and Microanalysis (CMM), The University of Queensland for the facilities and technical assistance.

Author contributions K. M.: writing—review and editing, writing—original draft, visualisation, validation, software, methodology, investigation, formal analysis, data curation, conceptualization. M. Z.: writing—review and editing, supervision, resources, project administration, methodology, funding acquisition. Q. T. and R. K.: writing—review and editing, supervision, project administration, methodology, investigation, formal analysis, conceptualization. All authors contributed to the methodology, reviewing and revising the manuscript.

Funding Open Access funding enabled and organized by CAUL and its Member Institutions.

Data availability No datasets were generated or analysed during the current study.

Declarations

Competing interests The authors declare no competing interests.

Open Access This article is licensed under a Creative Commons Attribution 4.0 International License, which permits use, sharing, adaptation, distribution and reproduction in any medium or format, as long as you give appropriate credit to the original author(s) and the source, provide a link to the Creative Commons licence, and indicate if changes were made. The images or other third party material in this article are included in the article's Creative Commons licence, unless indicated otherwise in a credit line to the material. If material is not included in the article's Creative Commons licence and your intended use is not permitted by statutory regulation or exceeds the permitted use, you will need to obtain permission directly from the copyright holder. To view a copy of this licence, visit <http://creativecommons.org/licenses/by/4.0/>.

References

1. Arun KL, Udhayakumar M, Radhika N (2022) A comprehensive review on various ceramic nanomaterial coatings over metallic substrates: applications, challenges and future trends. *J Bio Tribo-Corros* 9(1):11. <https://doi.org/10.1007/s40735-022-00717-6>
2. Hussain CM, Verma C, Aslam J, Aslam R, Zehra S (2003) *Handbook of corrosion engineering : modern theory, fundamentals and practical applications*, 1st ed. San Diego: Elsevier, <https://doi.org/10.1016/C2021-0-02205-7>
3. Haldhar R et al. (2023) “Smart anticorrosive materials: trends and opportunities,” pp. 45–60, <https://doi.org/10.1016/C2021-0-02413-5>
4. Bhadeshia HKDH, Honeycombe RWK (2024) *Steels: structure, properties, and design*, 5th ed. San Diego: Elsevier Science & Technology, <https://doi.org/10.1016/C2022-0-00193-8>
5. Marcuci JRJ, Souza ECd, Camilo CC, Lorenzo PLD, Rollo JMDdA (2014) Corrosion and microstructural characterization of martensitic stainless steels submitted to industrial thermal processes for use in surgical tools. *Rev Bras Eng Bioméd* 30(3):257–264. <https://doi.org/10.1590/rbeb.2014.025>
6. Wang YM et al (2018) Additively manufactured hierarchical stainless steels with high strength and ductility. *Nat Mater* 17(1):63–71. <https://doi.org/10.1038/nmat5021>
7. Saeidi K et al (2019) Ultra-high strength martensitic 420 stainless steel with high ductility. *Addit Manuf.* <https://doi.org/10.1016/j.addma.2019.100803>
8. Chatterjee S, Bhadeshia HKDH (2006) TRIP-assisted steels: cracking of high-carbon martensite. *Mater Sci Technol* 22(6):645–649. <https://doi.org/10.1179/174328406x86182>
9. Liu Y, Tang M, Hu Q, Zhang Y, Zhang L (2020) Densification behavior, microstructural evolution, and mechanical properties of TiC/AISI420 stainless steel composites fabricated by selective laser melting. *Mater Des.* <https://doi.org/10.1016/j.matdes.2019.108381>
10. Tran D et al (2024) Effects of TiN content and heat treatment on microstructural changes, mechanical strength, and corrosion resistance in selective laser melting of TiN/AISI 420 composites. *Mater Sci Eng, A.* <https://doi.org/10.1016/j.msea.2024.146438>
11. Yin Y, Tan Q, Bermingham M, Mo N, Zhang J, Zhang M-X (2022) Laser additive manufacturing of steels. *Int Mater Rev* 67(5):487–573. <https://doi.org/10.1080/09506608.2021.1983351>
12. Campbell CE, Stoudt MR, Zhang F (2020) “Additive Manufacturing of Steels and Stainless Steels,” in *Additive Manufacturing Processes*, pp. 346–365, <https://doi.org/10.31399/asm.hb.v24.a0006566>
13. Li K et al (2023) Additive manufacturing of ultra-high strength steels: a review. *J Alloys Compd.* <https://doi.org/10.1016/j.jallcom.2023.171390>

14. Zhang D, Liu A, Yin B, Wen P (2022) Additive manufacturing of duplex stainless steels - a critical review. *J Manuf Process* 73:496–517. <https://doi.org/10.1016/j.jmapro.2021.11.036>
15. Tan Q et al (2024) High performance plain carbon steels obtained through 3D-printing. *Nat Commun* 15(1):10077. <https://doi.org/10.1038/s41467-024-54507-4>
16. Tran D, Lin C-K, Tung P-C, Ho J-R, Le T-L (2024) Enhancing mechanical properties of selective-laser-melting TiN/AISI 420 composites through Taguchi GRA and PCA multi-response optimization. *J Mater Res Technol* 29:1278–1292. <https://doi.org/10.1016/j.jmrt.2024.01.174>
17. Zhu X, Li S, Yin T, Lu C, Liu X (2023) Influence of intrinsic manufacturing defects on corrosion behavior of AISI 420 stainless steel fabricated by laser powder bed fusion. *Electrochim Acta*. <https://doi.org/10.1016/j.electacta.2023.143067>
18. Shahriari A et al (2021) Corrosion resistance of 13wt.% Cr martensitic stainless steels: additively manufactured CX versus wrought Ni-containing AISI 420. *Corros Sci*. <https://doi.org/10.1016/j.corsci.2021.109362>
19. Shahriari A, Samei J, Sanjari M, Jahanbakht M, Amirkhiz BS, Mohammadi M (2022) Plastic injection molding dies using hybrid additively manufactured 420/CX stainless steels: electrochemical considerations. *NPJ Mater Degrad*. <https://doi.org/10.1038/s41529-022-00280-y>
20. Yang JR, Yu TH, Wang CH (2006) Martensitic transformations in AISI 440C stainless steel. *Mater Sci Eng A* 438–440:276–280. <https://doi.org/10.1016/j.msea.2006.02.098>
21. Dossett J, Totten GE (2014) Heat treating of martensitic stainless steels. *Heat Treat Irons Steels* <https://doi.org/10.31399/asm.hb.v04d.a0005985>
22. Rodríguez VM, López-Morelos VH, Nadimpalli VK, Pedersen DB, Ruiz A, Somers MAJ (2023) Effect of heat treatment processes on the microstructure and mechanical properties of spray-formed 440C martensitic stainless steel. *Steel Res Int*. <https://doi.org/10.1002/srin.202200749>
23. Salih AA, Omar MZ, Syarif J, Sajuri Z (2012) "An investigation on the microstructure and mechanical properties of quenched and tempered SS440C martensitic stainless steel. *Int J Mech Mater Eng* 7(2):119–123, 2012. [Online]. Available: <https://www.scopus.com/inward/record.uri?eid=2-s2.0-84866649397&partnerID=40&md5=087c82a4b663f8c6df6b738f9b13f6ca>
24. Salleh SH, Omar MZ, Syarif J, Ghazali MJ, Abdullah S, Sajuri Z (2009) Investigation of microstructure and properties of 440C martensitic stainless steel. *Int J Mech Mater Eng* 4(2):123–126. [Online]. Available: <https://www.scopus.com/inward/record.uri?eid=2-s2.0-73149108626&partnerID=40&md5=a5b5d9b5f79037d2fec57e4d158acf33>
25. Kwok CT, Lo KH, Cheng FT, Man HC (2003) Effect of processing conditions on the corrosion performance of laser surface-melted AISI 440C martensitic stainless steel. *Surface Coat Technol* 166(2):221–230. [https://doi.org/10.1016/S0257-8972\(02\)00782-X](https://doi.org/10.1016/S0257-8972(02)00782-X)
26. Idayan A, Gnanavelbabu A, Rajkumar K (2014) Influence of deep cryogenic treatment on the mechanical properties of AISI 440C bearing steel. *Procedia Eng* 97:1683–1691. <https://doi.org/10.1016/j.proeng.2014.12.319>
27. Syarif J, Yousuf MH, Sajuri Z, Baghdadi AH, Merabtene M, Omar MZ (2020) Effect of partial solution treatment temperature on microstructure and tensile properties of 440C martensitic stainless steel. *Metals*. <https://doi.org/10.3390/met10050694>
28. Bang GB et al (2022) Microstructural and mechanical properties of AISI 440C stainless steel fabricated using selective laser melting. *Mater Sci Eng A*. <https://doi.org/10.1016/j.msea.2022.144259>
29. Gatoes D, Alves R, Alves B, Vieira MT (2022) Selective laser melting and mechanical properties of stainless steels. *Materials* 15(21):7575. <https://doi.org/10.3390/ma15217575>
30. Pan Z et al (2024) Microstructural characterization of AISI 440C stainless tool steel fabricated by laser powder bed fusion. *IOP Conf Ser Mater Sci Eng*. <https://doi.org/10.1088/1757-899X/1310/1/012037>
31. Cui C et al (2023) Gas Atomization of Duplex Stainless Steel Powder for Laser Powder Bed Fusion. *Materials* (Basel). <https://doi.org/10.3390/ma16010435>
32. Özbilen S (1999) Satellite formation mechanism in gas atomised powders. *Powder Metall* 42(1):70–78. <https://doi.org/10.1179/pom.1999.42.1.70>
33. Toenjes A, Schmidt J, Hesselmann M (2025) Processability of water atomized 410L steel with laser powder bed fusion. *Prog Addit Manuf* 10(9):6343–6351. <https://doi.org/10.1007/s40964-025-00979-9>
34. Barkia B et al (2020) On the origin of the high tensile strength and ductility of additively manufactured 316L stainless steel: multi-scale investigation. *J Mater Sci Technol* 41:209–218. <https://doi.org/10.1016/j.jmst.2019.09.017>
35. Saeidi K, Gao X, Zhong Y, Shen ZJ (2015) Hardened austenite steel with columnar sub-grain structure formed by laser melting. *Mater Sci Eng, A* 625:221–229. <https://doi.org/10.1016/j.msea.2014.12.018>
36. Chen H, Gu D, Dai D, Ma C, Xia M (2017) Microstructure and composition homogeneity, tensile property, and underlying thermal physical mechanism of selective laser melting tool steel parts. *Mater Sci Eng, A* 682:279–289. <https://doi.org/10.1016/j.msea.2016.11.047>
37. Ciftci N, Ellendt N, Coulthard G, Soares Barreto E, Mädler L, Uhlenwinkel V (2019) Novel cooling rate correlations in molten metal gas atomization. *Metall Mater Trans B* 50(2):666–677. <https://doi.org/10.1007/s11663-019-01508-0>
38. Koshiya S, Kimoto K (2017) Improvement of effective solid angle using virtual-pivot holder and large EDS detector. *Micron* 93:52–56. <https://doi.org/10.1016/j.micron.2016.11.010>
39. Mu S, Rafaelsen J (2021) Mitigating shadowing and topographic artifacts using dual EDS detectors. *Microscopy Microanal*. <https://doi.org/10.1017/s143192762100581x>
40. Lei X, Feng Y, Zhang J, Fu A, Yin C, Macdonald DD (2016) Impact of reversed austenite on the pitting corrosion behavior of super 13Cr martensitic stainless steel. *Electrochim Acta* 191:640–650. <https://doi.org/10.1016/j.electacta.2016.01.094>
41. Hatem A, Schulz C, Schlaefel T, Boobhun JT, Stanford N, Hall C (2021) Influence of laser absorption by water- and gas-atomised powder feedstock on laser metal deposition of AISI 431 stainless steel. *Addit Manuf*. <https://doi.org/10.1016/j.addma.2021.102242>
42. Liu ZH, Zhang DQ, Chua CK, Leong KF (2013) Crystal structure analysis of M2 high speed steel parts produced by selective laser melting. *Mater Charact* 84:72–80. <https://doi.org/10.1016/j.matchar.2013.07.010>
43. Eisazadeh H, Khadka S, Wang X, Yuya P (2024) A comparative study of the mechanical characteristics of additively and conventionally fabricated 17–4 precipitation hardened stainless steel. *Prog Addit Manuf* 9(6):2445–2463. <https://doi.org/10.1007/s40964-024-00591-3>
44. Bhadeshia H, Honeycombe R (2017) Heat treatment of steels: hardenability," in steels: microstructure and properties, pp. 217–236. <https://doi.org/10.1016/B978-0-08-100270-4.00008-1>
45. Platl J, Leitner H, Turk C, Schnitzer R (2020) Determination of martensite start temperature of high-speed steels based on thermodynamic calculations. *Steel Res Int*. <https://doi.org/10.1002/srin.202000063>
46. Freeman FSHB, Sharp J, Xi J, Todd I (2019) Influence of solidification cell structure on the martensitic transformation in additively manufactured steels. *Addit Manuf*. <https://doi.org/10.1016/j.addma.2019.100917>

47. Cui C et al (2021) In situ x-ray diffraction analysis of microstructure evolution during deep cryogenic treatment and tempering of tool steels. *Steel Res Int*. <https://doi.org/10.1002/srin.202100076>
48. Kalsi NS, Sehgal R, Sharma VS (2010) Cryogenic treatment of tool materials: a review. *Mater Manuf Process* 25(10):1077–1100. <https://doi.org/10.1080/10426911003720862>
49. Weber N, Wohninsland A, Huber J, Tetzlaff T, Pfaff A (2025) Enhancing material performance by controlling retained austenite in laser powder bed fused 17–4PH steel. *Prog Addit Manufactur*. <https://doi.org/10.1007/s40964-025-01067-8>
50. Bhadeshia H, Honeycombe R (2017) Formation of martensite," in *Steels: Microstructure and Properties*, 2017, pp. 135–177, <https://doi.org/10.1016/B978-075068084-4/50007-8>
51. Hossain R, Pahlevani F, Quadir MZ, Sahajwalla V (2016) Stability of retained austenite in high carbon steel under compressive stress: an investigation from macro to nano scale. *Sci Rep* 6(1):34958. <https://doi.org/10.1038/srep34958>
52. Hosseini N, Forouzan F, Vuorinen E (2022) In-situ microstructural evolution during quenching and partitioning of a high-carbon steel by high-temperature X-ray diffraction. *Mater Today Commun*. <https://doi.org/10.1016/j.mtcomm.2022.103503>
53. Zhou CA, Sun Q, Qian D, Liu J, Sun J, Sun Z (2022) Effect of deep cryogenic treatment on mechanical properties and residual stress of AlSi10Mg alloy fabricated by laser powder bed fusion. *J Mater Process Technol* 303:117543. <https://doi.org/10.1016/j.jmatprotec.2022.117543>
54. Li K et al (2023) A comparative study on WE43 magnesium alloy fabricated by laser powder bed fusion coupled with deep cryogenic treatment: evolution in microstructure and mechanical properties. *Addit Manuf*. <https://doi.org/10.1016/j.addma.2023.103814>
55. Lashgari HR, Kong C, Adabifiroozjaei E, Li S (2020) Microstructure, post thermal treatment response, and tribological properties of 3D printed 17–4 PH stainless steel. *Wear*. <https://doi.org/10.1016/j.wear.2020.203367>
56. Tan Q et al (2024) Unravelling the roles of TiN-nanoparticle inoculant in additively manufactured 316 stainless steel. *J Mater Sci Technol* 175:153–169. <https://doi.org/10.1016/j.jmst.2023.08.018>
57. García-Hernández C et al (2024) Enhancing wear performance: a comparative study of traditional vs. additive manufacturing techniques for 17–4pH SS. *Wear*. <https://doi.org/10.1016/j.wear.2024.205258>
58. Iakovakis E, Avcu E, Roy MJ, Gee M, Matthews A (2022) Wear resistance of an additively manufactured high-carbon martensitic stainless steel. *Sci Rep* 12(1):12554. <https://doi.org/10.1038/s41598-022-15621-9>
59. Ryan MP, Williams DE, Chater RJ, Hutton BM, McPhail DS (2002) Why stainless steel corrodes. *Nature* 415(6873):770–774. <https://doi.org/10.1038/415770a>
60. Siqueira JS, de Abreu Alves MR, Luiz TM, Renzetti RA (2021) Effect of heat treatment on the chromium-depleted zones of a high carbon martensitic stainless steel. *Mater Corros* 72(11):1752–1761. <https://doi.org/10.1002/maco.202112483>

Publisher's Note Springer Nature remains neutral with regard to jurisdictional claims in published maps and institutional affiliations.